MODELLING AND PERFORMANCE ANALYSIS OF A NEW CONCEPT OF INTEGRAL COLLECTOR STORAGE (ICS) WITH PHASE CHANGE MATERIAL

Matteo Bilardo, Gilles Fraisse, Mickael Pailha, Enrico Fabrizio

MODELLING AND PERFORMANCE ANALYSIS OF A NEW CONCEPT OF INTEGRAL COLLECTOR STORAGE (ICS) WITH PHASE CHANGE MATERIAL

Matteo Bilardo[2,*], Gilles Fraisse[1], Mickael Pailha[1], Enrico Fabrizio[2]

[1]Univ. Grenoble Alpes, Univ. Savoie Mont Blanc, CNRS, LOCIE, 73000 Chambéry, France
[2]Politecnico di Torino. DENERG – Department of Energy, Corso Duca degli Abruzzi, 24, 10129 Torino, Italy

**Corresponding author: bilardo.matteo@gmail.com*

Abstract

Solar Domestic Hot Water (SDHW) systems represent a constantly evolving technology in today's applications. With the new directives promoted by the European Union the renewable energy share produced in buildings will tend to increase further. Research on how to increase the efficiency of the thermal production from renewable energy are therefore of the foremost importance. This study aims to investigate the energy performance of an integral collector storage (ICS) prototype for DHW production. This ICS represents a new concept technology, integrating inside the same device a flat plate absorber and a storage section with phase change material (PCM) connected by heat pipes filled with methanol. An objective of this study was to investigate a possible alternative to conventional solar systems, with the aim of reducing investment costs and improving system reliability without compromising energy performance. The energy assessment was carried out using a numerical model in the Engineering Equation Solver (EES) environment, following an electrical analogy scheme. After a validation process by means of experimental data, a yearly simulation was launched in order to estimate the productivity and the solar fraction of the prototype. The results obtained allowed a global energy evaluation and a comparison with similar systems and to identify the pros and cons of this new technology.

Nomenclature

Abbreviations

ICS	Integral collector storage
PEG	Polyethylene glycol
HP	Heat pipe
DHW	Domestic hot water
EES	Engineering Equation Solver

Variables

C	Thermal capacity ($J.K^{-1}$)
c_p	Specific thermal capacity ($J.K^{-1}kg^{-1}$)
E	Solar radiation ($W.m^{-2}$)
e	Thickness (m)
h_e	External heat transfer coefficient ($W.m^{-2}.K^{-1}$)
R	Thermal resistance ($K.W^{-1}$)
S	Absorber area (m^2)
S_{HC}	Single honeycomb cell area (m^2)
T	Temperature (K)
U_{HP}	Heat transfer coefficient for one heat pipe ($W.K^{-1}$)

Greek letters

α_{glass}	Glass absorption coefficient (-)
λ	Thermal conductivity ($W.m^{-1}.K^{-1}$)
φ_{DHW}	Heat flux for DHW production (W)
φ_{HP}	Heat flux transferred by heat pipes (W)

Indices

abs	Absorber
x	Layer
la	Air gap
eva	Evaporator
cond	Condenser
pe	Front cavity plate
pi	Back cavity plate
ar	Back side
ext	External
in	Inlet
out	Outlet
ve	External glass surface
vi	Internal glass surface
ae	Absorber front side
ai	Absorber back side
i	Insulation

1. Introduction

The energy exploitation of non-renewable resources is now a consolidated problem for humankinds (IEA, 2018a). In spite of an increasing awareness of this issue, the use of modern renewable resources is currently on 10.4% of total final energy consumption across the world (REN21, 2018). The rational use of energy, as well as the introduction of new renewable systems, therefore represents a challenge of primary importance.

Among the renewable resources available, solar energy is certainly the resource that can be exploited most easily and in a higher quantity compared to other sustainable sources. Solar radiation can be intensively exploited in large production plants or at the domestic level through installations aimed to be used by small groups of people. This feature allows solar energy to acquire added value and to be used on both the large and small scales. Solar thermal power has grown steadily since 2000, when the total installed power was not quite 50 GW, reaching 326 GW installed in 2013 (REN21, 2014).

The use of solar energy for thermal purposes, for both domestic hot water production and household heating, is one of the most used renewable solutions adopted in the world (Ge et al., 2017). Recently, the European Union recast the Energy Performance of Buildings Directive (EPBD), setting the rules toward a low-emission EU building stock by 2050 and the decarbonisation of existing buildings (European Union, 2018), encouraging for the first time the implementation of smart control and automation systems to increase existing buildings efficiency. The technologies of solar thermal production are now widespread in the most varied applications, both industrial and residential, and many countries require a mandatory installation in new buildings.

1.1. State of the art on Integral Collector Storages

In the solar domestic hot water (SDHW) systems market, technological research is in continuous development. Most solar energy systems for DHW production include an absorber connected to a storage tank, usually filled by water. These classic systems have some disadvantages such as space consumption, complexity of installation and the use of various auxiliary elements i.e. circulation pumps, which can negatively affect the operation of the system, both in terms of performance and maintenance. To cope with these problems, numerous alternative solutions have been studied, for DHW production as well as for space heating (Robinson and Sharp, 2015). Integral collector storages (ICS) represent a valid SDHW answer to conventional systems (Smyth et al., 2006). An ICS encloses the solar absorber and the storage section inside a single casing, thus generating a single device with reduced dimensions, easy architectural integration and without auxiliary elements. ICS represent a very large family of solar collectors. The coupling of a solar absorber with a thermal storage can generate numerous possible combinations, grouped into several main categories as shown in Figure 1. A first group of combinations can be made according to how the solar energy is captured, separating the concentrating collectors from the non-concentrating collectors (Singh et al., 2016). In non-concentration collectors the absorber communicates directly or indirectly with the storage. Flat-plate integrated collector storage (FPICS) and the tank type ICS, in which the storage section itself acts as an absorber, are placed in this category. Direct FPICSs foresee a direct contact between the absorber and the storage. Recently, Kumar and Rosen (2010) studied the performances of an ICS with a corrugated surface absorber, in direct contact with a water storage installed on the back of the device. On the other hand, AL-Khaffajy and Mossad (2013) verified the potential of an indirect ICS that uses different designs of a heat exchanger, which connected the absorbing surface with a water storage tank.

Several ICS systems solutions involve the implementation of a solar collector with tanks or boxes, using water as a means of thermal storage. Already in 1975, Garg (1975) developed a rectangular prototype capable of supplying 90 l of water at a temperature between 50 and 60 °C in winter conditions with a desert climate. Recently, Dharuman et al. (2006) studied a solar water heater with a capacity of 130 l under different operating conditions. A screen insulation was applied to this solution to counteract night-time thermal losses. Further ICS systems consist in the coupling of the solar collector with heat storages of a particular design. This category includes the triangular-shaped solar water heater designed by Ecevit et al. (1989) and tested in different volume configurations during a 24-hour cycle. The same triangular geometric shape was subsequently taken up by Kaushik et al. (1994) to increase the natural convection and the heat exchange between the collector and water in the storage. The ability to produce hot water was tested by the authors during the hours of maximum solar activity, studying the behaviour of the collector in northern latitudes under winter condition. Despite being isolated on all sides, the prototype undergoes significant thermal losses during the night, due to the lack of insulation behind the collector section, in direct contact with the thermal storage. Another particular design has been carefully studied by Cruz et al. (2002), who has verified both experimentally and through a numerical model the effect of thermal stratification in an ICS coupled with a trapezoidal storage. The prototype designed by the authors had as main objective to be as cheap as possible and was studied in a typically Mediterranean climate. Also in this case, the thermal insulation is placed around the storage section, leaving however the surface behind the solar collector without insulation.

Indirect systems have also been tested in space heating applications. Robinson et al. (2013) assessed the benefits of a solar wall transferring heat to the indoor environment by means of heat pipes connecting the absorber to a water tank installed in a room of a building. A similar approach, involving heat pipes, was used by Esen and Esen (2005), in designing a thermosyphon two-phase solar collector and testing different HTF inside the heat pipe.

With regard to concentrating collectors, the most widespread are the parabolic concentrating compounds (CPC) types. This technology makes it possible to reflect and concentrate the solar radiation directly on the surface of the absorber, reaching temperatures above 200°C (Singh et al., 2016). Already twenty years ago, (Souliotis and Tripanagnostopoulos, 2004) analysed several models of CPC integrated with a horizontal storage tank, on which the solar radiation was converged, reaching storage temperatures over 70 °C. These authors also proposed a comparison between similar CPCs but with different mounting characteristics, comparing CPCs with horizontal and vertical storage tanks, and concluded that while horizontal tanks have better average performance in thermal temperature rise and thermal losses, vertical storage tanks present a better thermal stratification (Tripanagnostopoulos and Souliotis, 2004). A similarly designed solution inspired Helal et al. (2011), who verified the performance of a CPC composed of three parabolic branches to produce domestic hot water for an average household user. In contrast, Kumar et al. (2010) developed a concentration type ICS with the shape of a truncated pyramid, with the main purpose of being used as a tool for cooking in poor countries. Although very different from standard solar collectors, the tests conducted by the authors have revealed an interesting potential for the development of this technology.

Furthermore, an intriguing technological aspect concerning the ICS is the use of a thermal storage medium that is alternative to water, such as phase change materials (PCM). The use of phase change materials makes it possible to extend the storage capacity and to make the thermal energy available for a longer period of time, including night time energy needs. The implementation of PCM also makes it possible to avoid problems related to the use of bulky water tanks, limiting the space occupied and reducing costs. Given the large number of phase change materials on the market, a challenging aspect of using this technology is certainly the multitude of applications in which it can be implemented. This scenario refers to systems for DHW production, and extends also to the internal thermal comfort control of household heating. (Haillot et al., 2011) carefully studied and modelled (Haillot et al., 2012) an innovative storage composite made up of compressed expanded natural graphite (CENG) and phase change material (PCM) for ICS application. In addition to the purposes related to space heating, ICSs have often been used for the most disparate applications, as demonstrated by the recent studies of Khan (2016) focused on solar water distillation using phase change materials. In this study, different composites have been tested, demonstrating the effectiveness of PCMs in this type of application. Another solution sometimes implemented in PCM systems is to form special mixtures of phase change material with other liquids, such as water. This leads to the formation of particular slurries, which can be pumped and used in special hydraulic systems, significantly increasing the thermal storage capacity of the final fluid (Serale et al., 2015).

The scheme of Figure 1 summarizes all the cited works concerning the main categories of Integral Collector Storages in the literature.

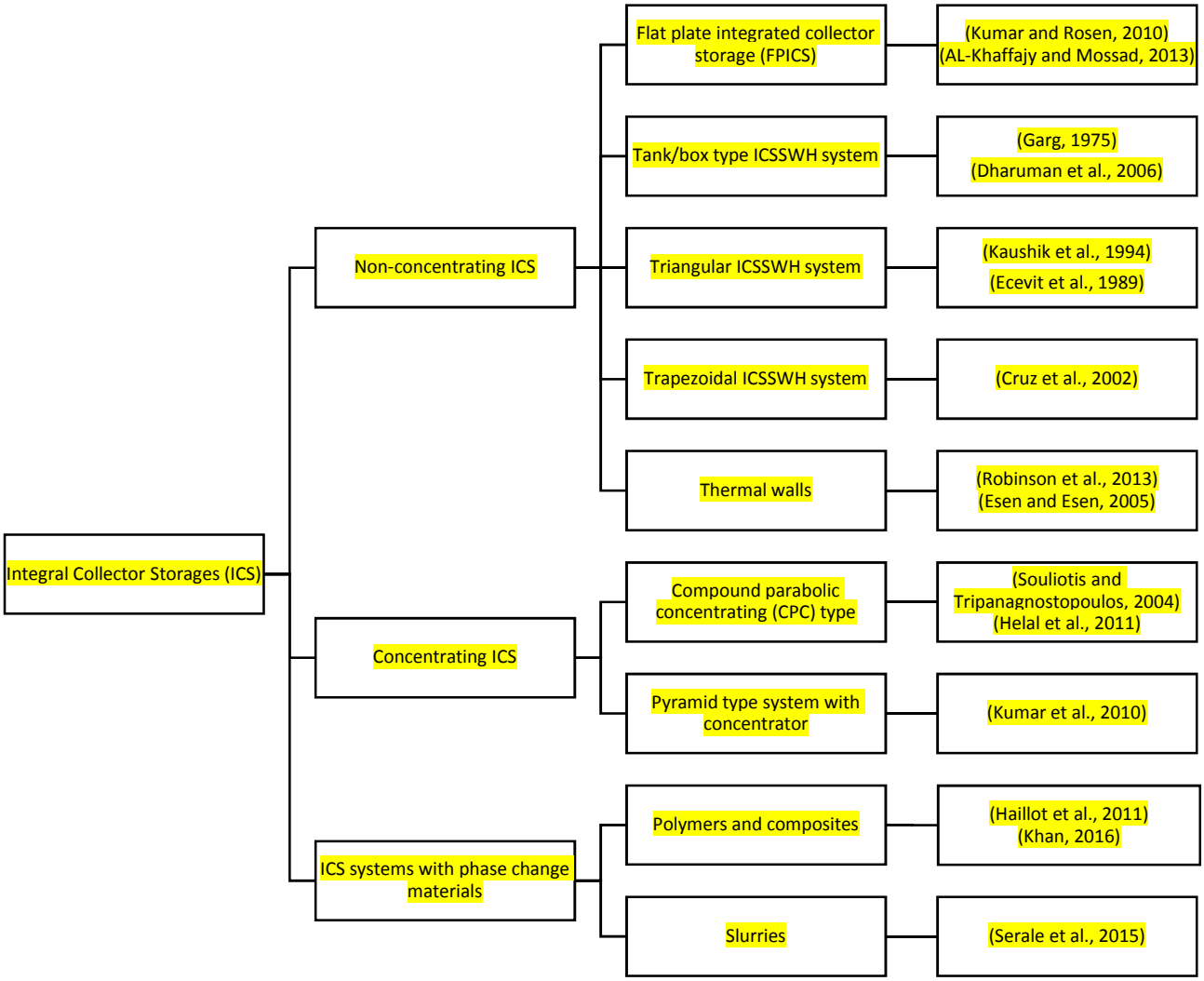

Figure 1 - Main types of ICS based on the classification made by Singh et al. (2016)

The main issue shared by the majority of ICSs concerns thermal losses, especially suffered during night time (Singh et al., 2016). Since this type of collectors provides a single device installed in outdoor environments, thermal losses, especially during the night, represent a primary problem in developing this technology. Where possible, ICSs require a specifically designed thermal insulation, in order to preserve the heat stored during the day. Furthermore, the proximity of the absorber to the storage section makes the impact of this problem even more evident. To address this problem, it is necessary to pay attention both to the thermal storage and to the way in which it communicates with the absorber. The object of this study is the analysis of an innovative prototype of ICS that was designed with the aim of solving the problems just addressed, coupling a fully insulated PCM storage cavity and a flat-plat collector within the same casing.

1.2. Aim of the work

Based on the analysis of the state of the art and considering the limits present in most of the studies on the ICSs carried out so far, the purpose of the work presented in this work is the study of the energy performance of a new ICS concept able to:

- minimize the thermal losses related to the night-time hours during which the storage is not used;

- reduce maintenance operations through a self-adjusting system devoid of mechanical parts;
- have high performance in terms of energy storage, making it suitable for typically cold climates;
- have a low impact architectural integration maintaining a small area covered in a contained weight.

In addition to representing the main features on which the design of the prototype was developed, these elements represent the innovative aspects with that might overcome the shortcomings of the systems already studied.

In this study, the energy performances of this new ICS concept have been specially studied. To evaluate the potential of the prototype in a general way, a numerical model was developed that simulates its behaviour. In the first part of the work a numerical model was developed, following an electrical analogy approach, and subsequently validated by means of experimental data collected before. The second part of the study was dedicated to simulating the model yearly performance, with the aim of evaluating its global potential.

2. The new concept

The case study prototype is an ICS that combines a traditional flat-plate collector with a storage cavity containing phase change material (PCM) (Fraisse and Pailha, 2016). The whole system is presented as a single block of aluminium inside which all the components necessary to ensure correct operation have been installed. Figure 2 shows the prototype on which the experimental tests were conducted.

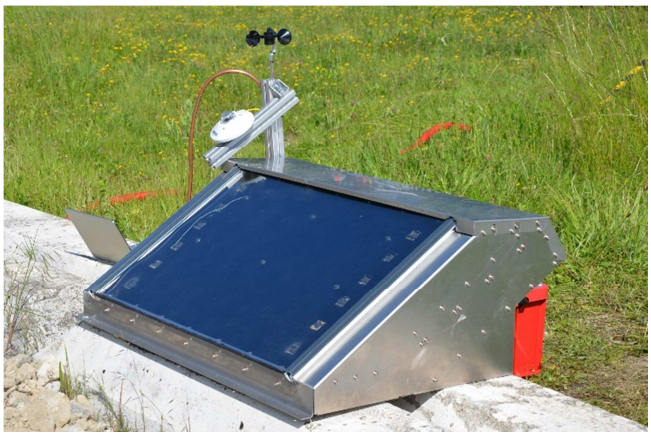

Figure 2 - Experimental prototype setup

The peculiarity of the system, which makes it unique in its kind, is the mechanism by which the absorber section and the storage cavity have been put into communication: between them six heat pipes filled with methanol have been designed with the task of removing the heat absorbed by the collector and transferring it towards the storage section, positioned on the back. The heat pipes have been designed and installed with a slight inclination (5°), operating in natural convection due to gravity. Finally, the DHW production occurs instantaneously through a copper coil welded to the front plate of the cavity and extracts the heat when water flows inside the pipe. All the elements just described have subsequently been isolated and enclosed within a single casing (Figure 3).

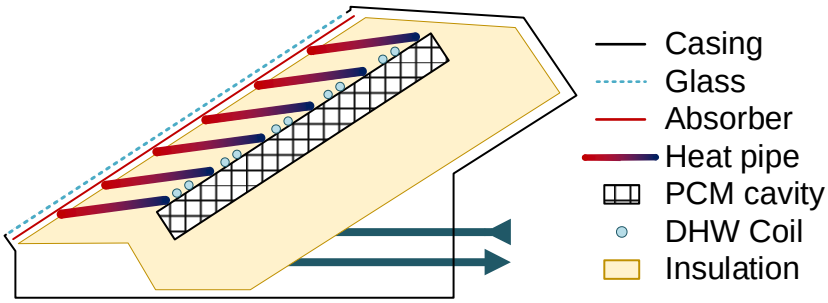

Figure 3 - ICS prototype

Similar systems present in the literature involving heat pipes or PCM storages (D'Avignon and Kummert, 2016; Esen and Esen, 2005; Serale et al., 2015) confirmed that a prototype of ICS with the above characteristics had never been realized. The prototype therefore represents a new concept of ICS for DHW production intended to integrate the traditional flat-plate collector with three other main elements:

1) **Heat pipes** filled with methanol, used as a means of transferring heat from the absorber surface to the storage section. The use of the heat pipes, being installed with a slight inclination, foresees the operation with a thermosiphon mechanism. The expected result is a high thermal heat exchange, as well as the effect of a thermal diode (Susheela & Sharp, 2001).
2) Storage section by means of a cavity containing **PCM**. In order to achieve better energy and structural performance, the cavity has been designed as an aluminium structure made of honeycomb cells, inside which the phase change material has been arranged (Hasse, Grenet, Bontemps, Dendievel, & Sallée, 2011). This also made it possible to reduce the storage thickness, reducing the overall dimensions of the ICS. Among various possibilities, the polyethylene glycol 6000 (PEG 6000) has been chosen as storage medium due to its thermal properties such as the melting range (52/66 °C), suitable for DHW production.
3) Total **thermal insulation** of all elements within the same casing. This choice, combined with the installation of the heat pipes, allows to obtain a storage section completely isolated on all its sides, possibly reaching the thermal capacities of a classic storage with an insulated water tank.

Four different heat exchanges occur within the prototype (Figure 4). A first heat flow involves the heat pipes, using methanol inside them as a heat-transfer fluid. A second heat exchange occurs at the condenser side of the heat pipe, where the heat is transferred to the storage cavity. Finally, domestic hot water heating can take place either through the transfer of the heat stored in the PCM, or through a direct exchange between the condenser and the copper coil of the DHW, both welded on the same aluminium plate.

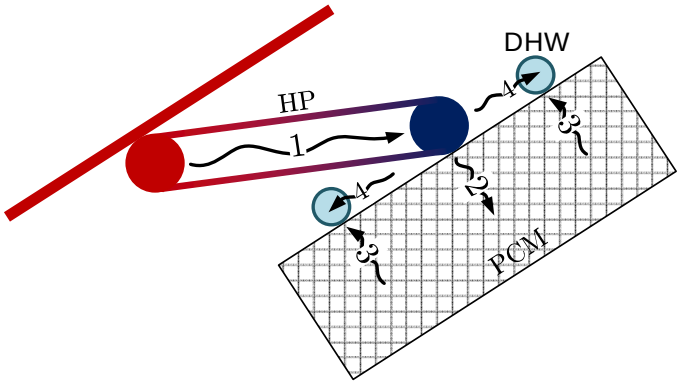

Figure 4 - Principe of operation and main heat fluxes

3. Modeling of the ICS

The numerical model was developed following an electrical analogy. Due to the general complexity and the high number of components, all the elements except the cavity have been modelled following a one-dimensional approach. For the PCM cavity a different procedure has been performed, preferring a two-dimensional model, better simulating its real behaviour. For each internal component, the energy balances were pointed out, creating a rather complex system of differential equations. The ICS has been modelled into the EES (Engineering Equation Solver) environment, an equation-solver program able to numerically solve nonlinear algebraic and differential equations. The early modelling phase was subsequently followed by an optimization phase, integrated in the same program, with the aim to improve the reliability of the model, especially regarding unknown parameters.

3.1. Model description using electrical analogy

Figure 5 presents the prototype's scheme according to which the model was built. With the exception of the PCM cavity, every layer is considered one dimensional. For this reason, temperatures at nodes (identified by black dots) are supposed to be constant along the surface normal to solar radiation, in the y direction. One the other hand, the PCM cavity, together with the aluminium plates, is discretized into 21 separates nodes (7 in the x direction, 3 in the y direction), generating a two-dimensional pattern (Haillot, Nepveu, Goetz, Py, & Benabdelkarim, 2012). While the x-axis represents the main direction, normal to the absorber plane, the y-axis indicates a direction parallel to the prototype width. The choice to adopt a hybrid model is due to different factors. The one-dimensional model that describes all the sections of the collector going from its external surface to the storage cavity simplifies the computational cost without leading to serious discrepancies with respect to reality, as already demonstrated in numerous studies(Azzolin et al., 2018; Carmona and Palacio, 2019). The same approach cannot be adopted for the PCM cavity since the geometry of the honeycomb cells induces a temperature gradient both in the axial direction (x in Figure 5) and in the radial direction (y in Figure 5), even though the gradient is lower in the radial direction. Furthermore, a two-dimensional model allows to better describe the heat transfer mechanism inside the cells: given the small size of the single cell, convection indeed is not the dominant heat transfer mechanism, especially when the PCM is in liquid phase. These peculiar characteristics of the system to be modelled have therefore led to the development of a two-dimensional model, considering the rotation axis of each single honeycomb cell (Bony and Citherlet, 2007; Haillot et al., 2012).

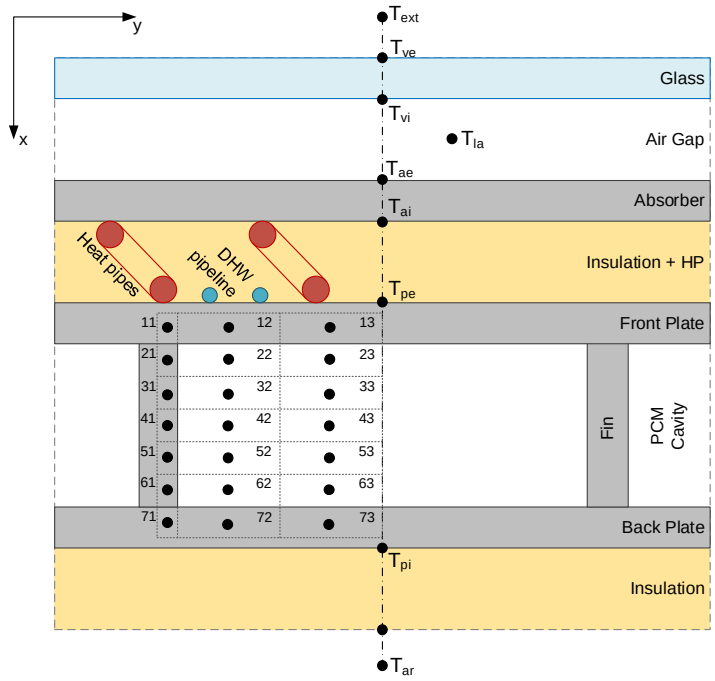

Figure 5 - ICS model scheme with sections and temperature nodes (black dots)

At each identified temperature node an energy balance is performed. Starting from the glass layer in contact with the outside air, at the T_{ve} node the following energy balance was set:

$$h_e \cdot (T_{ext} - T_{ve}) + \alpha_{glass} \cdot E = \frac{T_{ve} - T_{vi}}{\frac{e_{glass}}{\lambda_{glass}}} \left[\frac{W}{m^2}\right]. \quad (1)$$

With the same procedure the following layers, including the air gap, the absorber and the insulating material have been modelled. For these components thermal conductivity and thickness were considered while thermal capacity was neglected, developing a series of equations similar to (1).

After the first insulation layer heat pipes have to be modelled. Heat flux across them is modelled according to the conductance U_{HP}, setting the relation:

$$\varphi_{HP} = U_{HP} * \Delta T_{HP}\ [W], \quad (2)$$

where ΔT_{HP} is the temperature difference between the evaporator and the condenser of the heat pipe. To simplify the model these temperatures are supposed to be equal to the contact surface temperatures where they are installed. According to this hypothesis, the evaporator temperature is equal to T_{ai} (absorber backside temperature) whereas the condenser temperature equals T_{pe}. Regarding the conductance coefficient U_{HP}, a constant value for the model has been chosen after an experimental analysis previously carried out (Nemec et al., 2011). Even though a constant U_{HP} value is a significant approximation for the model, this hypothesis allows to save a considerable computational cost, without compromising the simulation results, especially during large simulation time scenarios. A more detailed model, considering a variable conductance as a function of the heat pipe wall temperature was also considered (Rudy & Manuse, 2016). However, the accuracy of the results that were obtained does not justify the larger computational cost of the model.

Besides the useful flux provided from the heat pipes, losses have been considered too. An additional heat flow ($\varphi_{HP,TB}$), depending on the temperature difference between the evaporator and the condenser, was supposed to be lost by the heat pipes, taking into consideration the unavoidable thermal bridge that is generated.

$$\varphi_{\mathrm{HP,TB}} = TB_{HP} * \Delta T_{HP}\ [W]. \quad (3)$$

To describe the thermal bridge effect across the heat pipe profile, the constant coefficient TB_{HP} is introduced in Eq. (3). Based on the geometric shape of the heat pipes, the coefficient was computed according to the equation:

$$TB_{HP} = \lambda_{copper} * \pi * \left(\frac{D_e^2 - D_i^2}{4 * e_i}\right)\left[\frac{W}{°C}\right], \quad (4)$$

where D_e and D_i are the external and internal pipe diameters and λ_{copper} is the copper thermal conductivity.

The two heat flows involved in the modelling of the heat pipe have been integrated into the electrical analogy as thermal resistances in parallel to that generated by the insulating material layer. Figure 6 shows a detail of the electrical analogy for the examined layer, where the model of the heat pipe is enclosed between the temperature node that represents the back side of the absorber (T_{ai}) and the temperature of the front cavity plate (T_{pe}).

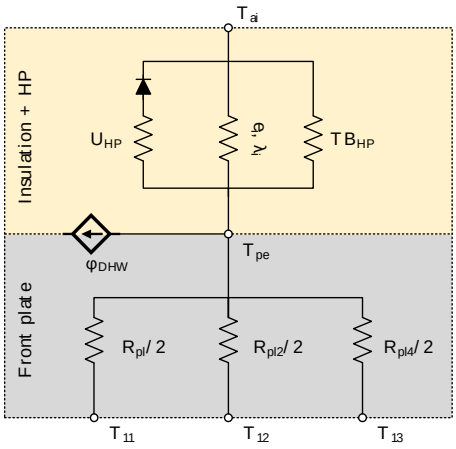

Figure 6 -Electrical analogy of T_{pe} node

The cavity front plate represents a critical node of the model because it is the point where the 1D scheme becomes two-dimensional: the cavity front plate, being part of the storage, is in fact divided into three separate nodes. Moreover, the complexity of the model increases further since the DHW production coil is installed around the same node.

DHW pipeline has been modelled following its geometrical shape and considering a mean temperature for the water flowing inside. Moreover, the surface temperature of the DHW pipeline has been considered equal to the front plate temperature (T_{pe}), since these two components are welded together. The heat flux exchanged by forced convection is linked to the pipeline internal temperature and the water temperature flowing inside, according to the formula:

$$\varphi_{DHW} = \pi \cdot D_{i,DHW} \cdot L_{DHW} \cdot h_{c,DHW} \cdot \left(T_{si,DHW} - T_{mean,w}\right)\ [W], \quad (5)$$

where D_i and L are respectively the internal diameter and the pipeline length while h_c is the heat transfer coefficient. The latter was computed from the Nusselt number, according to the type of state, turbulent or laminar:

$$h_{c,DHW} = \lambda_w \cdot \frac{Nu}{D_{i,DHW}}\ \left[\frac{W}{m^2 \cdot °C}\right], \quad (6)$$

where

$$Nu = \begin{cases} Nu_{lam} = 3{,}66 + 0{,}0668 \cdot \left[\dfrac{Re \cdot Pr \cdot \frac{D_{i,DHW}}{L_{DHW}}}{1 + 0{,}04 \cdot \left(Re \cdot Pr \cdot \frac{D_{i,DHW}}{L_{DHW}} \right)^{2/3}} \right] \\ Nu_{turb} = 0{,}023 \cdot \mathrm{Pr}^{1/3} \cdot Re^{0{,}8} \end{cases}. \quad (7)$$

The same heat exchanged by conduction throughout the pipeline walls is:

$$\varphi_{DHW} = \dot{m}_w \cdot c_{p,w} \cdot \left(T_{w,out} - T_{w,in}\right) [W], \quad (8)$$

where $\left(T_{w,out} - T_{w,in}\right)$ is the water temperature difference between the pipeline inlet and the outlet.

In order to improve the model performance and simulate a real behaviour for a possible building implementation, a 3-way valve was added to the model with the task to keep the outlet water temperature below 55 °C, mixing the water coming out from the solar collector with by-passed cold water from the main network.

To recap, DHW coli, heat pipes, front cavity plant and insulation layer are considered in the energy balance set around the node T_{pe}, thus resulting in the following equation:

$$\frac{T_{ai} - T_{pe}}{\frac{e_i}{\lambda_i}} \cdot S_{HC} + \left[\#_{HP} \cdot \varphi_{HP} + \#_{HP} \cdot TB_{HP} \cdot \left(T_{ai} - T_{pe}\right) - \varphi_{DHW} \right] \cdot \frac{S_{HC}}{S} = \frac{T_{pe} - T_{11}}{\frac{R_{pl}}{2}} + \frac{T_{pe} - T_{12}}{\frac{R_{pl2}}{2}} + \frac{T_{pe} - T_{13}}{\frac{R_{pl4}}{2}} [W]. \quad (9)$$

Considering the PCM cavity, the honeycomb structure containing PEG6000 was modelled together with the aluminium front and back plates as well as the fin. Figure 7 describes the PCM cavity mesh, modelled taking advantage of its symmetrical shape. The spatial discretization of the cavity is based on a sample cell, and its thermal behaviour has been normalized to the honeycomb cell section. The 2D mesh counts 21 temperatures nodes (6 for the plates, 5 for the fin and 10 for the PCM) including the front cavity aluminium plate, the PCM itself, the aluminium fin that spaces the honeycomb structure and the aluminium plate at the back. The aluminium plates at the front and the back are included in the first and last layers of the mash in y direction, while the fin develops just along the x direction. The rest is filled by the PCM.

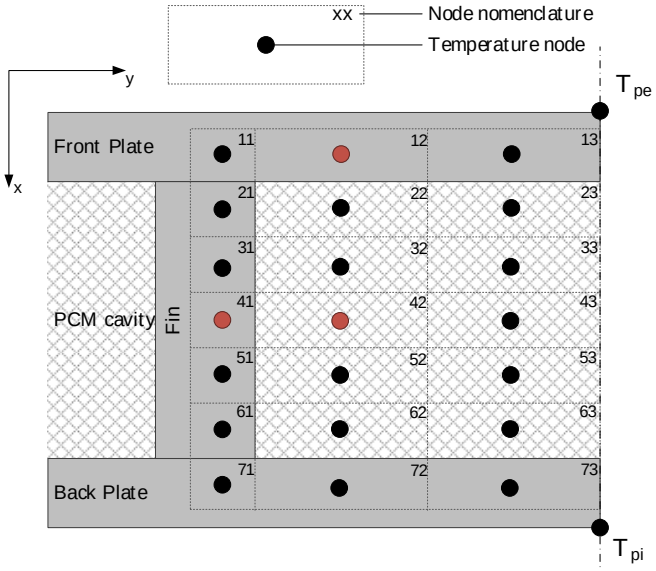

Figure 7 - PCM cavity mesh

The temperature nodes represented by the T_{pe} and T_{pi} are the connecting point between the 1D model and the 2D mesh. Solving the energy balances set on these nodes, temperatures can be

determined. These two temperatures have a singular meaning because they will be used to validate the model, giving comparable values with the experimental data. In the experimental setup, thermocouples have been installed right in both locations to monitor the cavity temperature, since the PCM itself was sealed inside the cavity and cannot be accessed. The plate temperatures are therefore the best comparison method between the numerical model and the experimental data.

Figure 8 focuses on the cavity back plate and shows how the electrical scheme of the 2D cavity mesh is connected with the rest of the one-dimensional model. In the back plate the DHW coil is no longer present and the cavity is separated from the external environment only by the layer of insulating material. As previously done for the front plate, an energy balance has been set for the back plate in the same way, giving the following relation:

$$S_{HC} \cdot \left[\frac{T_{pi} - T_{AR}}{\frac{e_i}{\lambda_i} + \frac{1}{h_{eAR}}}\right] = \frac{T_{pi} - T_{71}}{\frac{R_{pl}}{2}} + \frac{T_{pi} - T_{72}}{\frac{R_{pl2}}{2}} + \frac{T_{pi} - T_{73}}{\frac{R_{pl4}}{2}} \; [W]. \qquad (10)$$

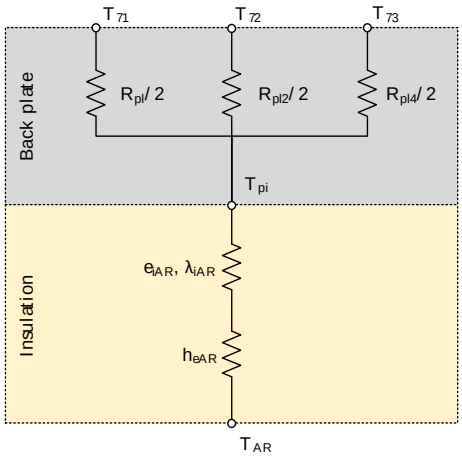

Figure 8 - Electrical analogy of T_{pi} node

Inside the cavity, the heat stored into the PCM is simulated by a capacitor, using the heat capacity C as the fundamental quantity, computed as:

$$C = c_p \cdot \rho \cdot V \quad \left[\frac{J}{°C}\right]. \qquad (11)$$

In addition to this, heat capacity is also considered for the aluminium plates, while it has been neglected for the fin. Energy balances are set at each of the 21 nodes to solve the temperature pattern inside the cavity, giving to each node the related heat capacity value depending on whether it is a PCM or an aluminium plate node. The specific thermal capacity c_p will assume a constant value in the case of aluminium, while its value will depend on the temperature when the PCM is examined, as explained in section 3.2. Between each cell composing the mesh, specific thermal resistances have been computed to better simulate the actual thermal behaviour. According to the cylindrical geometry of the honeycomb, several radii were set to describe the cell distance from the symmetry axes.

Therefore, thermal resistances in y (r) direction are

$$R_{th,r} = \frac{\ln\left(\frac{r_o}{r_i}\right)}{2 * \pi * L * k} \quad \left[\frac{°C}{W}\right]. \tag{12}$$

On the other hand, thermal resistances following x axes direction are

$$R_{th,x} = \frac{L}{k * A} \quad \left[\frac{°C}{W}\right]. \tag{13}$$

In both cases, L is the length, k is the thermal conductivity (PCM or aluminium) and A is the surface considered. Figure A-1 in the Annex summarizes the electrical scheme of the cavity. All the energy balances set at the temperature nodes inside the cavity took into consideration thermal resistances and thermal capacities. The equations (14), (15), (16) represent the balances for the three types of nodes modelled, respectively the aluminium plate, the PCM layer and the fin cell. The position of these temperature nodes inside the mesh can be identified from Figure 7, where the red dots indicate the nodes whose energy balances are:

T_{12} (aluminium plate layer):

$$C_{12} \cdot \frac{dT_{12}}{dt} = \frac{T_{11} - T_{12}}{R_{pl1}} + \frac{T_{13} - T_{12}}{R_{pl3}} + \frac{T_{22} - T_{12}}{\frac{R_{pl2}}{2} + \frac{R_{PCM1}}{2}} + \frac{T_{pe} - T_{12}}{\frac{R_{pl2}}{2}} \ [W]. \tag{14}$$

T_{42} (PCM layer):

$$C_{42} \cdot \frac{dT_{42}}{dt} = \frac{T_{41} - T_{42}}{R_{PCM} + R_{ail2}} + \frac{T_{43} - T_{42}}{R_{PCM2}} + \frac{T_{32} - T_{42}}{R_{PCM1}} + \frac{T_{52} - T_{42}}{R_{PCM1}} \ [W]. \tag{15}$$

T_{41} (fin cell):

$$0 = \frac{T_{31} - T_{41}}{R_{ail}} + \frac{T_{51} - T_{41}}{R_{ail}} + \frac{T_{42} - T_{41}}{R_{ail2} + R_{PCM}} \ [W]. \tag{16}$$

3.2. Phase change modelling

To describe the thermal behaviour of the phase change material, a differential scanning calorimeter (DSC) analysis was developed, with the aim of determining the specific heat trend as a function of the PCM temperature, as well as melting and crystallization ranges. The DSC analysis is an established tool in the analysis of the thermal and chemical behaviour of materials. It evaluates the difference in the heat flux exchanged between a standard reference and a sample, PEG 6000 in this case study (Dumas et al., 2018). This evaluation is done with a constant heating or cooling rate over time. Solidification or melting processes can be studied separately, applying the most appropriate rate to the assessment of the phenomenon. Taking into consideration the real temperature variation inside the prototype, which in normal operation does not exceed 0.7 °C/h, the experimental analysis with the DSC analysis was performed with a heating and cooling rate equal to 1 °C/h. The curves obtained for the melting and crystallization phase are shown in Figure 9 with the dashed lines. Both were then fitted by applying the empirical relation proposed by Kuznik (Kuznik et al., 2008) according to the following equation, shown in the same figure with the solid black line.

$$c_p = \begin{cases} a + b \cdot e^{-\left(\frac{(T_f - T)}{4}\right)^2} \; if \; T \leq T_f \; \left[\frac{J}{g \cdot °C}\right] \\ a + b \cdot e^{-\left(\frac{(T_f - T)}{3}\right)^2} \; if \; T > T_f \; \left[\frac{J}{g \cdot °C}\right] \end{cases}, \tag{17}$$

where a and b are two characteristic parameters and T_f is the mean temperature to which fusion or crystallization occur. The DSC analysis and the subsequent study of the collected data made it possible to identify the characteristic parameters of the curves, as well as allowing greater accuracy regarding the fusion and crystallization ranges of the PCM. These data are collected in Table 1.

Table 1 - Thermal parameters from DSC analysis

Parameter	Value	Unit
Melting range	57-63	°C
T_f	61.66	°C
a	2.11	$J.g^{-1}.°C^{-1}$
b	58.08	$J.g^{-1}.°C^{-1}$
Crystallization range	42-50	°C
T_f	45.56	°C
a	2.28	$J.g^{-1}.°C^{-1}$
b	54.58	$J.g^{-1}.°C^{-1}$

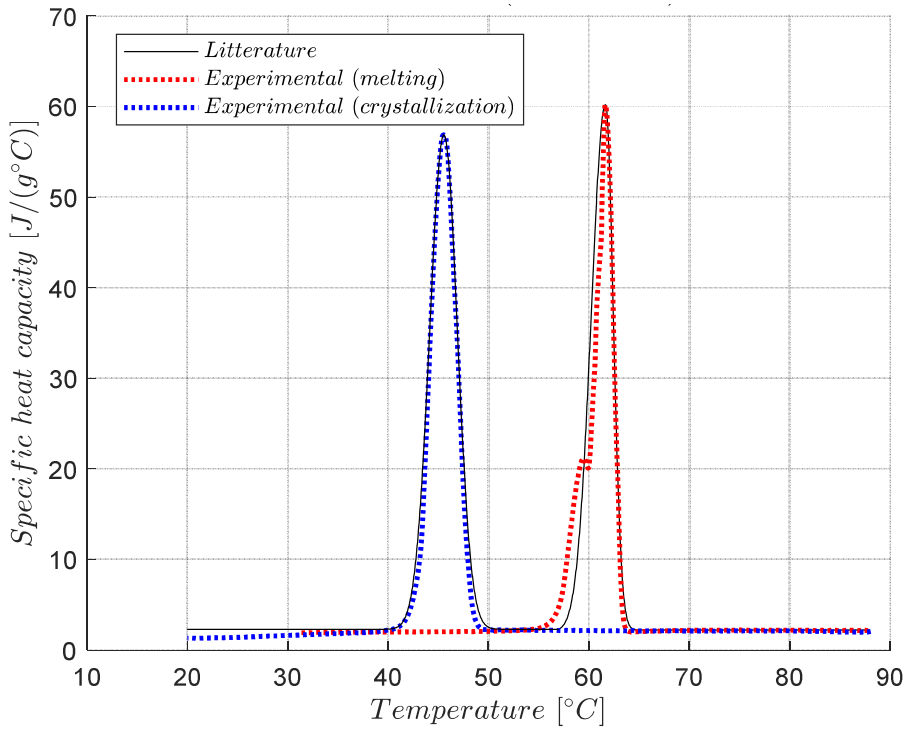

Figure 9 - Experimental PEG 6000 specific heat fitting from literature

Once the best fitted curves for both melting and freezing of the PCM were defined, interrupted cooling and heating phenomena were addressed. In fact, a specific model description is required when the PCM inside the cavity starts to melt and then is cooled down without reaching the 100% liquid phase. In this case, as well as in the opposite one, when the solidification procedure is interrupted, the c_p behaviour may be ambiguous. For this reason, a specific approach has been

used to describe interrupted heating and cooling phenomena based on the studies carried out by (Delcroix et al., 2015) and (D'Avignon and Kummert, 2016). According to them, when heating or cooling is stopped while the PCM goes through a phase transition, the specific heat curve (as well as the enthalpy curve) lies in between the melting and freezing ones.

Figure 10 and Figure 11 show the c_p curves implemented in the model when the melting or crystallization phases are interrupted. The red line describes the melting process, the blue one represents the freezing process and the dashed line describes the PCM c_p values during an interrupted heating or cooling process.

Considering Figure 10, PCM starts melting in point 1 (around 50 °C) and it is heated up to 60 °C (point 2) without reaching the complete liquid phase (over 65 °C approximately). Afterwards, PCM undergoes a cooling process and the value assumed by its specific heat does not lay neither on the melting curve nor on the freezing one but moves on an average curve (point 3). While cooling continues, specific heat follows the mean c_p curve (dashed black line) until the PCM is completely solid (point 4). From solid state, when heating conditions are applied again and the material starts melting, it will follow the standard melting red line. The same phenomenon happens in the opposite way when dealing with interrupted cooling (Figure 11).

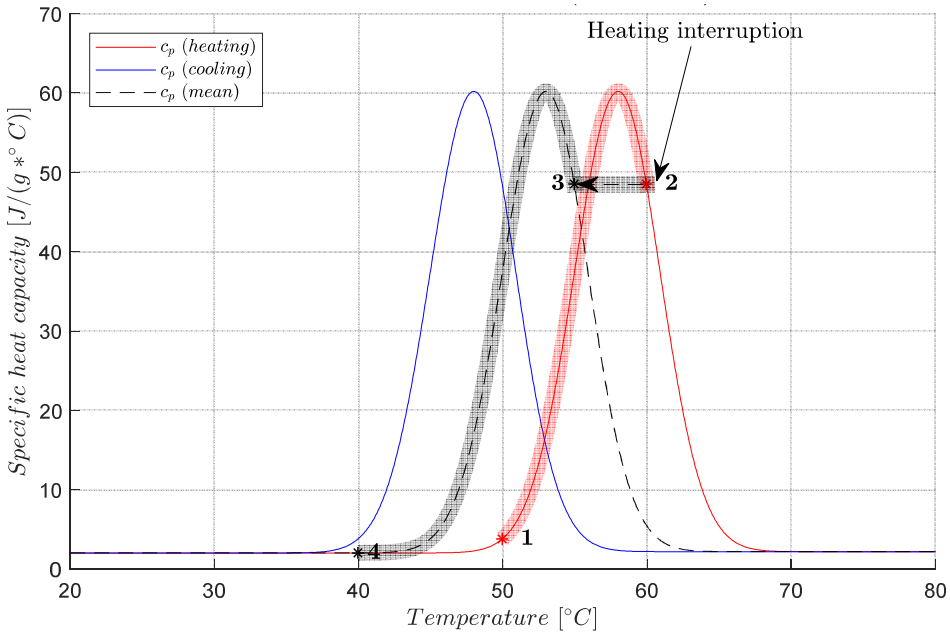

Figure 10 - Interrupted heating model for specific heat (Delcroix et al., 2015)

The opposite phenomenon, i.e. the interruption cooling process, is described by an analogous numerical model and shown in Figure 9. When the PCM is in a complete liquid phase (point 1) and starts to be cooled down, its specific heat curve follows the one obtained through the DSC analysis (blue line). When the cooling process is stopped before the PCM had reached the solid state (point 2) and is heated up, c_p trend will follow the average curve (black line) as in the interrupted heating phenomenon.

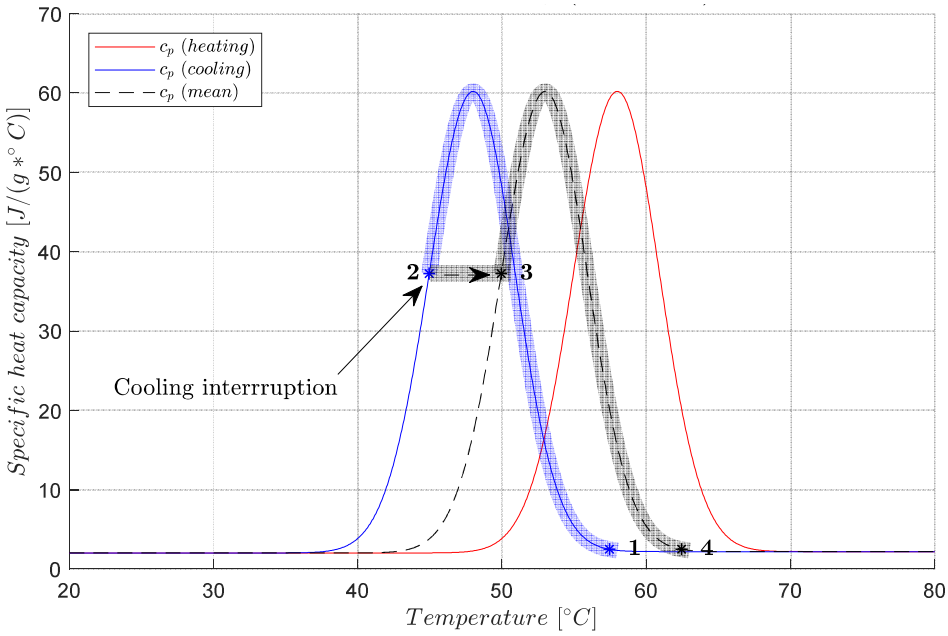

Figure 11 - Interrupted cooling model for specific heat (Delcroix et al., 2015)

All the energy balances equations just presented and used to describe the physical behaviour of the prototype have been implemented in the EES environment, forming a system of non-linear equations that are solved simultaneously by the software.

4. Model validation

4.1. Input and boundary conditions

The model was initially validated according to real experimental data collected on site. For this scope the external temperature, solar radiation, cold water temperature and water flow rate were used as direct inputs for the model, running short time simulations corresponding to the experimental data collected. In addition, the starting temperature for the PCM cavity was set equal to the experimental one. The main output values provided by the model are the trend of the internal temperatures identified by the temperature nodes established in the model, and the production temperature of the domestic hot water (Figure 12). The main objective of this first set of simulations was to create a valid and reliable model with respect to the actual operation of the prototype.

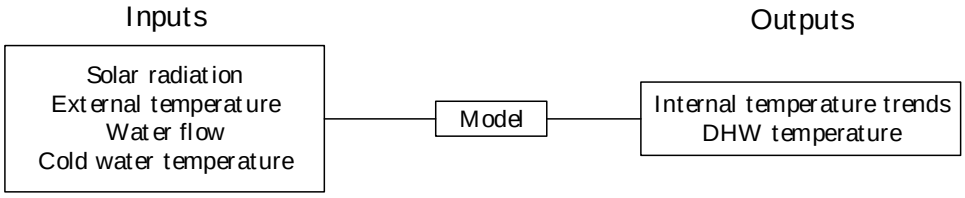

Figure 12 - Inputs and outputs to perform model validation

The collection of experimental data took place directly on the test bench set up for the study of the prototype, shown in Figure 13. To monitor the internal temperatures, 25 K-type thermocouples, with an accuracy of ±0.1 °C, were installed. Thermocouples were assembled into two groups, so as to group the cold junctions into two isolated boxes, thus having a uniform reference temperature. Finally, a connection was made to the data acquisition unit, where the potential differences of each individual thermocouple have been saved, as well as the reference temperatures. The latter were measured with two PT100 thermoresistances applied directly in the two insulated boxes. The two reference temperatures indicate the temperature of the thermocouples' cold junctions. The value of this temperature is necessary for the subsequent data processing, which in the case of thermocouples consists of transforming the values of the potential difference into temperatures. Moreover, the use of insulated boxes allows not only to group together all the 25 thermocouples installed inside the prototype, but also to maintain a uniform temperature of the cold junctions, a fundamental aspect since all the thermocouples have undergone a calibration process under similar conditions.

The experimental set-up is completed by a pyranometer (±20 W/m^2 accuracy) and an anemometer, to monitor weather conditions. Finally, a flow meter reads the waterflow that passes through the prototype. An Agilent 34972A data acquisition unit (Keysight Technologies), was installed to store experimental data collected on-site.

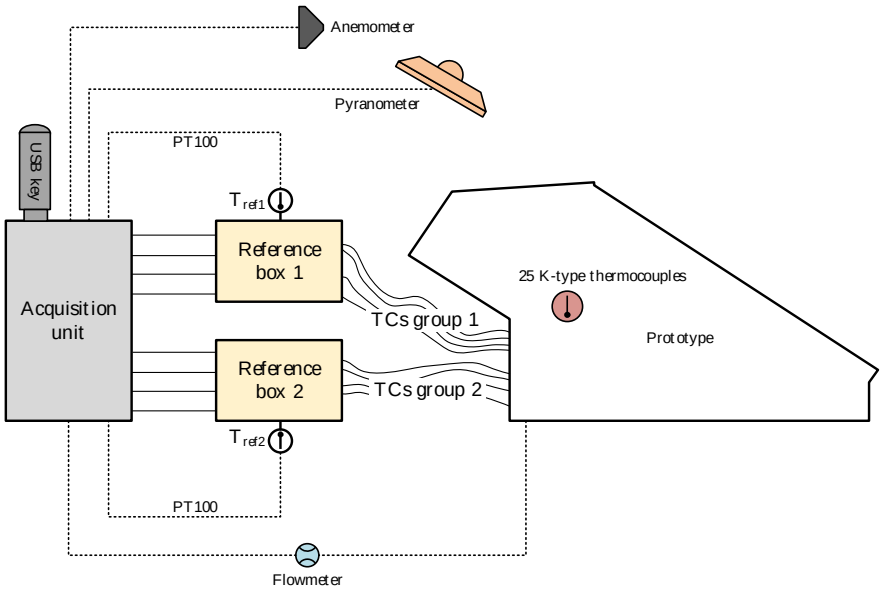

Figure 13 - Bench test set up

4.2. Validation process

Different weather conditions and operating mode have been considered to validate the model. The validation process involved on-site operation during two different periods of the year. Initially, the model was validated under summer condition, considering a typical summer week with a relatively high solar radiation. The same approach was then used to test the model's behaviour during a representative winter week. During both periods, standard operation without DHW collection was tested, allowing the cavity to perform normal heating and cooling cycles. DHW production was subsequently simulated, focusing on the cavity behaviour and its temperature drop. In order to get better results, different simulation timesteps were used depending on the experiment performed. Standard operation of the system was studied with a 30 seconds timestep, while for DHW production, requiring a faster-time comprehension, the timestep was reduced to 5 seconds. The same timestep used for simulating the model were adopted by the data acquisition system in the experimental bench.

During the validation process, temperature trends coming from the simulation results were compared with real data collected in the experimental bench. To verify the model without a water collection process, data analysis was focused to the absorber and cavity temperature, considered as the most relevant temperature nodes to prove model's reliability. Similarly, the same temperature trends were used to verify the DHW production simulation. However, in this case the attention was shifted to shorter period of time, emphasizing temperature drops when the water collection occurs.

Starting from summer weather condition, a typical week was analysed in Figure 14, showing normal operation without water collection. Absorber (T_{abs}) and inferior cavity plate (T_{pi}) were simulated and compared with the experimental data (solid line). The lower graph in the figure points out the actual solar radiation during the week (red solid line), showing an ordinary radiation behaviour. To verify the accuracy of the model, the standard deviation was evaluated for every validation data set, according to the formula:

$$\sigma T = \sqrt{\frac{\sum_{i=1}^{N}\left(T_{i,simulated} - T_{i,exp}\right)}{N}}\ [°C]. \qquad (18)$$

The results obtained are collected in Table 2. For summer performance σT does not exceed 5 °C neither for T_{abs} nor for T_{pi}.

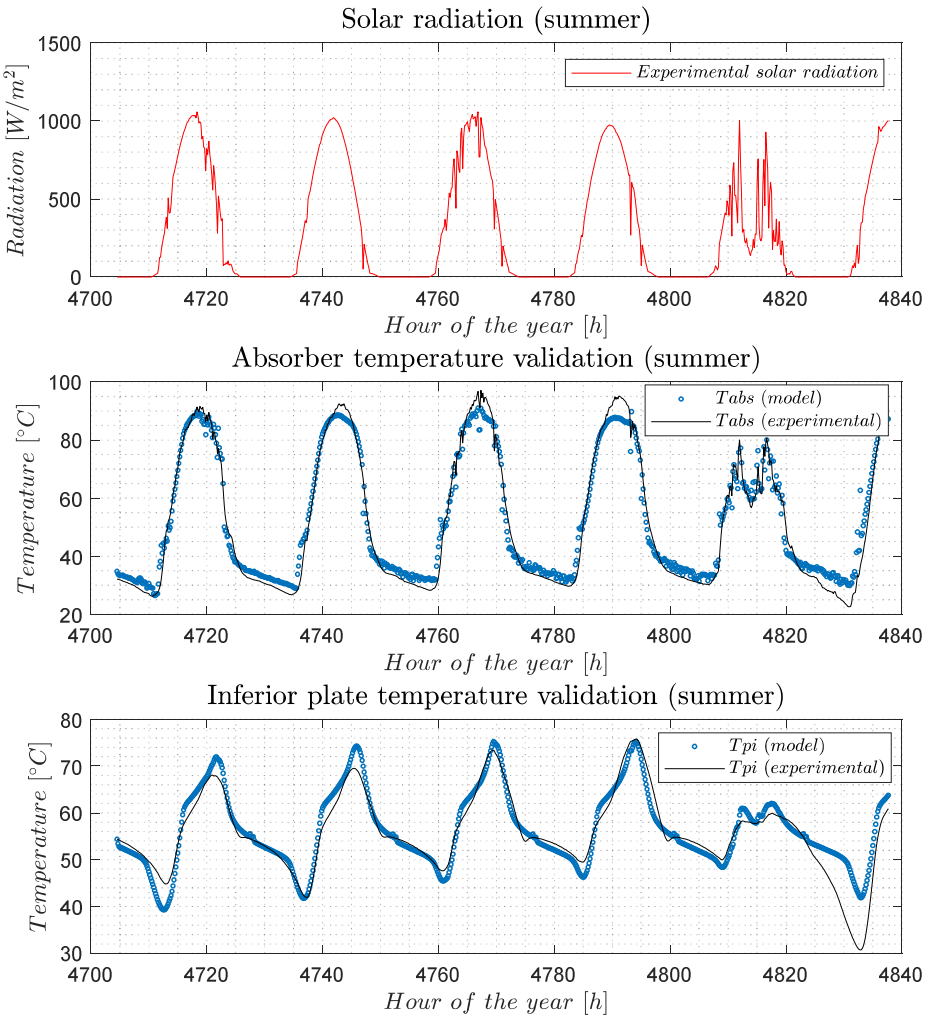

Figure 14 - Absorber (T_{abs}) and inferior cavity plate (T_{pi}) temperature simulation in a typical summer week with related solar radiation

During a summer typical day, the ability to produce hot water has been tested with a simple water collection from the collector pipeline. A water flowrate of 3.3 l/min for 20 minutes was extracted from the collector at 3:00 a.m. In Figure 15 the experimental data collected are compared to the simulated ones. Again, absorber and cavity temperature are shown. The absorber temperature trend suggests a rather reliable behaviour: the water collection process is well described, having a considerable impact on the absorber temperature. A similar effect can also be seen on the cavity temperature trend, which undergoes a considerable drop during the collection of water, even falling below 30 °C. A further potentiality of the studied prototype is however evidenced by the rapid temperature rise of the storage cavity. With a constant solar radiation, the PCM cavity manages to pass from 30 °C to 60 °C in a short time. This result indicates a lower heat capacity when the PCM goes across the solid state. This feature allows the system to reach DHW production temperatures in less time, thereby reducing the need for auxiliary heaters. The differences between the experimental temperature values and those generated by the numerical model can most probably be addressed to the complexity of the cavity plate. Furthermore, the experimental values used to validate the model come from different thermocouples applied on the experimental prototype and therefore represent local values of the internal components that were subsequently averaged. On the other hand, the numerical values generated by the model, in particular for the absorber and cavity plates, come from a one-dimensional simulation.

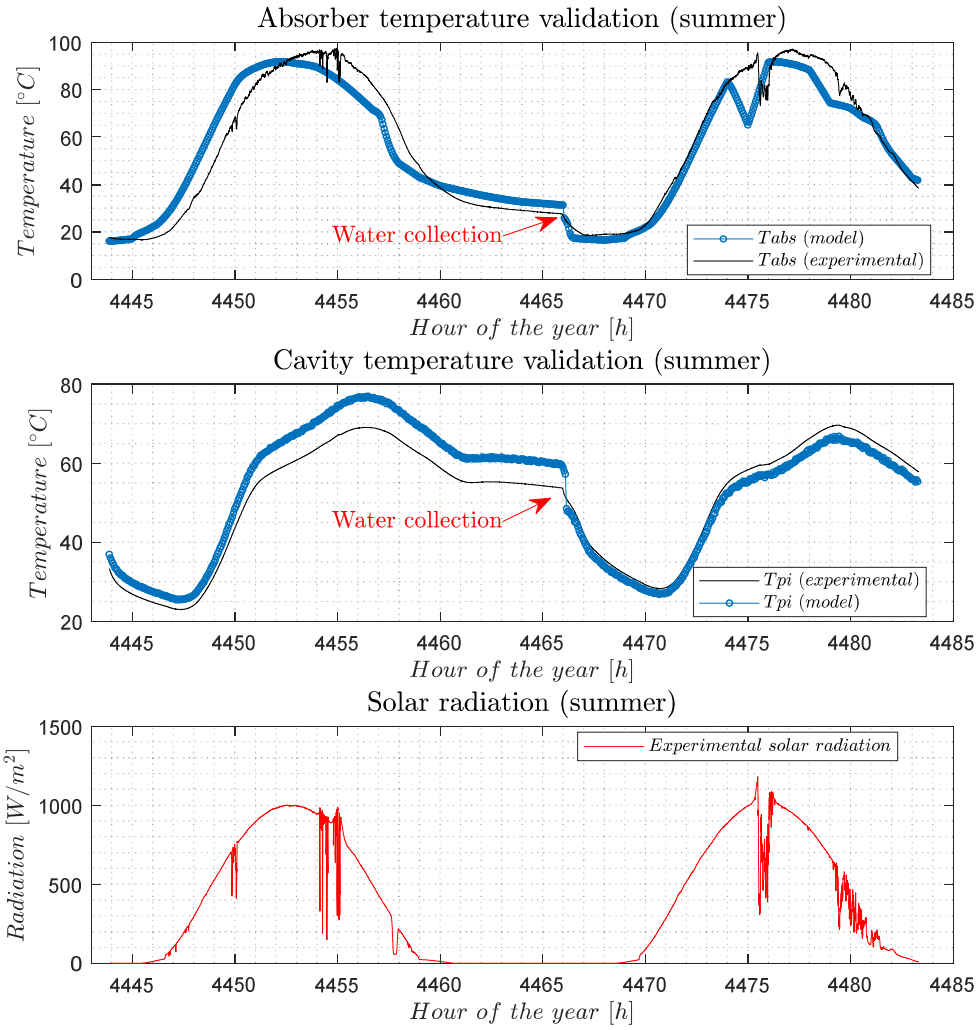

Figure 15 - Absorber (T_{abs}) and cavity (T_{pi}) temperature during summer water collection with related solar radiation

The validation process is continued by examining a typical winter week, subject to variable weather conditions. Figure 16 shows again absorber (T_{abs}) and cavity (T_{pi}) temperature comparison

between simulated and real data. As can be seen from the results obtained, due to very low external temperature condition, the PCM cavity never reaches the double phase region, involving just sensible heat stored in the cavity. Moreover, keeping the storage in the solid phase, heat transfer involves only conduction, with an almost constant value of specific heat. In these simplified conditions the model seems to provide results very similar to the real ones, especially for the cavity temperature, where simulated and real temperature are difficult to distinguish. Model's response to the solid phase state is very accurate, both with constant and discontinuous solar radiation, and this is confirmed by their standard deviation (Table 2). Considering the results obtained during previous simulations in summer conditions, is clear that the weakest point of the model is the phase change region, where the thermal behaviour of the cavity is harder to describe. Surely, further investigations might be dedicated to this aspect.

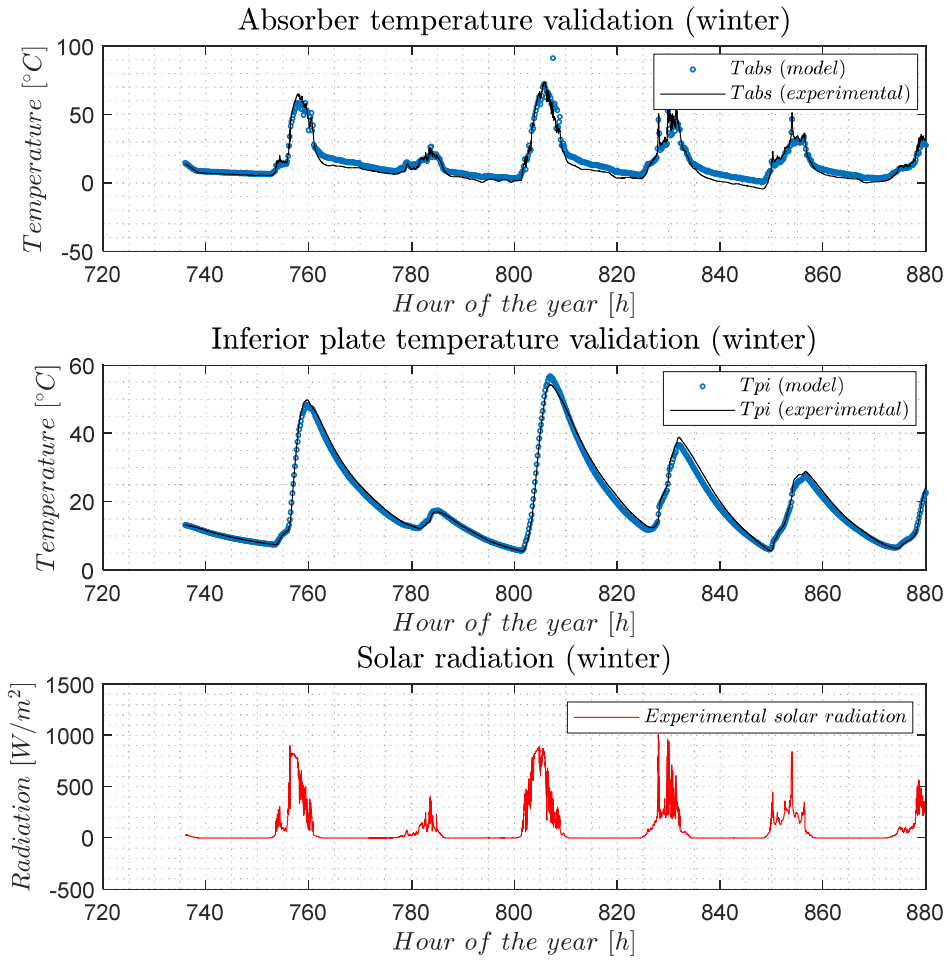

Figure 16 - Absorber (T_{abs}) and inferior cavity plate (T_{pi}) temperature simulation in a typical winter week with related solar radiation

The production of DHW has also been validated in winter weather conditions, reducing the waterflow to 0.35 l/min. Under these conditions, the validation of the model produced results very similar to the real ones, especially as regards the trend of cavity temperatures (T_{pi}), where the standard deviation is 2.45 °C (Table 2). Figure 17 shows the details of the water collection, comparing the actual data with the simulated data during a typical winter day.

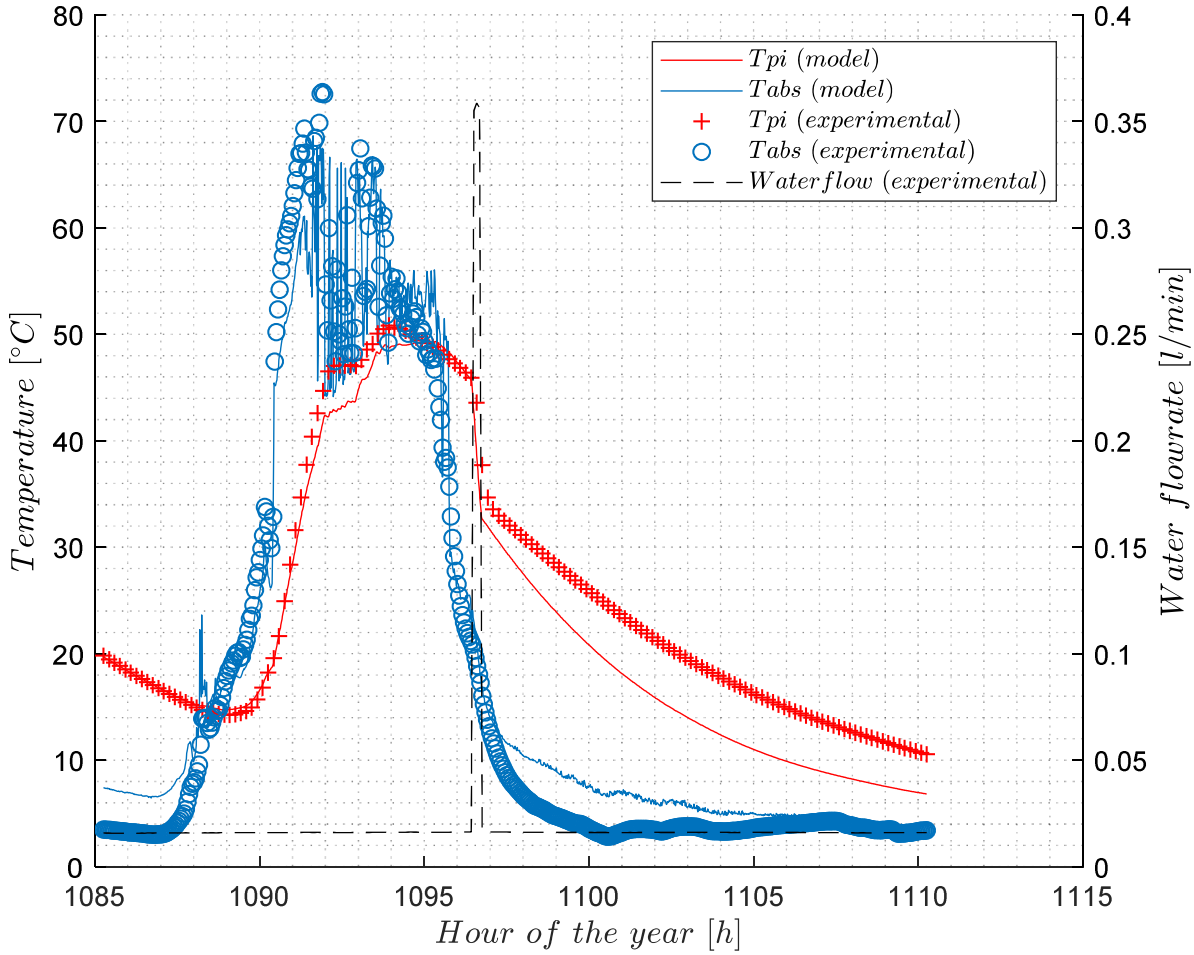

Figure 17 - Water collection simulation detail during winter

Table 2 - Standard deviation for absorber and back plate temperatures

Simulation	σT_{abs} [°C]	σT_{pi} [°C]
Summer without water collection	4.75	4.88
Summer with water collection	6.65	4.34
Winter without water collection	3.55	1.25
Winter with water collection	3.53	2.45

Overall, the numerical model confirms the real system operation, both in normal condition and during a water collection. Some inaccuracies may occur during the double phase region, when the phase change material inside the cavity passes through the melting phase. However, sub cooling phenomenon as well as interrupted heating and cooling seem to have been considered pretty well in the development of the model, giving reasonable results when they occur.

5. Yearly performance

Once the model was validated and its stability proved, a yearly simulation was run, with the aim of evaluating global energy performances of the prototype along the year. To evaluate the yearly productivity of the model, 6 prototypes of ICS in parallel were simulated, for a total absorbent surface equal to 3 m^2. As input data, a weather station in Chambéry, France, where the experimental study was carried out, provided mean meteorological data from the past ten years. Furthermore, cold water temperature at the DHW inlet is provided by French standards,

considering a monthly mean value from the climatic data of the 2012 national thermal regulation (RT2012) (Ministère de l'Egalité des Territoires et du Logement, 2013).

The daily DHW requirements set in the simulation of the model are defined by two water collections at different times of the day, one in the morning and another in the afternoon, reaching a total daily production of DHW equal to 120 litres. The waterflow flowing in the model is limited to 0.5 l/min, to ensure values similar to those tested during the model validation process.

A three-way valve operation has also been simulated (Figure 18), limiting the water outlet temperature to 55 °C by mixing the hot water produced by the ICS with cold water from the network. The purpose of the valve, not installed in the test bench, is to avoid the production of water above 55 °C, unusable for domestic purposes. The valve regulates the waterflow allowed to flow inside the prototype's model, maximizing it when the outlet temperature is less than 55 °C and reducing it when the DHW production temperature exceeds 55 °C. The time step used for the yearly simulation is 30 seconds.

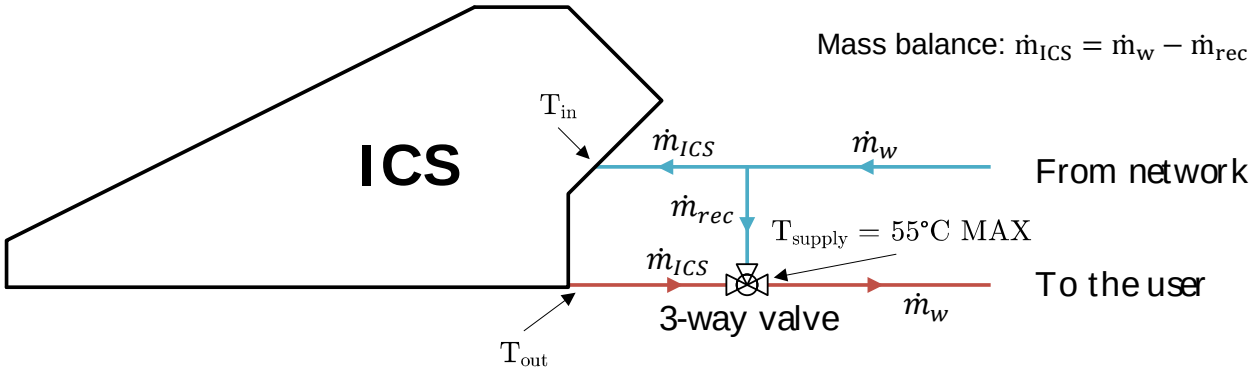

Figure 18 - 3-way valve operation simulated in model yearly performances with relater waterflows

5.1. Performance criteria

Two representative dimensionless parameters (solar and stored fraction) have been used to describe the prototype's overall performances (IEA, 2018), so that it could be comparable with other SDHW systems. However, some physical quantities such as the stored energy ((23) have been formulated specifically for the model developed, having no bibliographic references. The first key performance indicator is represented by the solar saving fraction f_{SOLAR} in Eq. (19), defined by the ratio between the amount of useful energy provided by the solar system and the total energy demanded by our DHW application:

$$f_{SOLAR} = \frac{E_{USEFUL}}{E_{DEMAND}} \; [-]. \qquad (19)$$

Solar fraction has been computed monthly, in order to show the performance trend during the year. Useful energy (20) has been calculated from the waterflow passing through the ICS ($\dot{m}_{ICS}$) and the temperature difference across the inlet and outlet of the DHW pipeline:

$$E_{USEFUL} = \int_{t_{in}}^{t_{end}} \left(\dot{m}_{ICS} \cdot c_{p,w} \cdot (T_{out} - T_{in}) \right) dt \; [J]. \qquad (20)$$

In contrast, the amount of demanded energy (21) was computed taking into account a fixed supply water temperature equal to 55 °C and the total waterflow coming from the network ($\dot{m}_w$):

$$E_{DEMAND} = \int_{t_{in}}^{t_{end}} \left(\dot{m}_w \cdot c_{p,w} \cdot (55 - T_{in}) \right) dt \ [J], \tag{21}$$

where $\dot{m}_w$ is the constant flow rate supplied to the user and fixed to 0.5 l/min.

The second key parameter chosen is the stored energy rate, defined as the energy stored in the cavity divided by the incident solar radiation on the absorber surface:

$$f_{STORED} = \frac{E_{STORED}}{E_{SOLAR}} \ [-]. \tag{22}$$

Stored energy has been computed ad-hoc for the project as the energy transferred from the absorber to the cavity by means of the heat pipes:

$$E_{STORED} = \int_{t_{in}}^{t_{end}} (\#_{HP} \cdot U_{HP} \cdot \Delta T_{HP}) dt \ [J]. \tag{23}$$

5.2. Simulation results

Figure 19 shows the cumulative values of the main energy vectors involved in the system defined by equations in section 5.1: the useful energy, the energy demanded, the stored energy and also the solar energy. The values shown are referred to a single unit of system simulated, made by an absorber surface equal to 0.5 m^2.

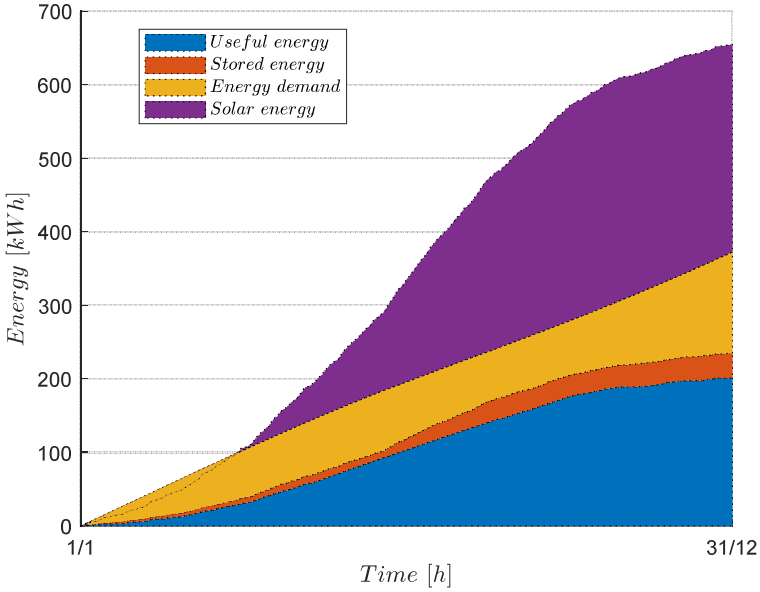

Figure 19 – Energies involved in the model yearly simulation for a single unit (A_{abs} = 0.5 m^2) during one-year simulation

The areas shown in the Figure 19 are not cumulative. Useful energy produced by the model (blue area) is not able to fully meet the yearly energy demand (yellow + orange + blue areas). The energy stored inside the model is represented by the sum between the orange and blue areas. The gap between stored and useful energy is relatively small (orange area), showing that most of the stored energy is used for the actual production of DHW. From the yearly simulation the DHW productivity of the prototype can be estimated, giving a result equal to 402.2 kWh/m^2 confirming that the ICS has a similar productivity to the one of conventional solar water heaters.

To have a general overview of the system's performance, the solar fraction f_{SOLAR} was evaluated following Eq. (20) and is reported in Figure 20.

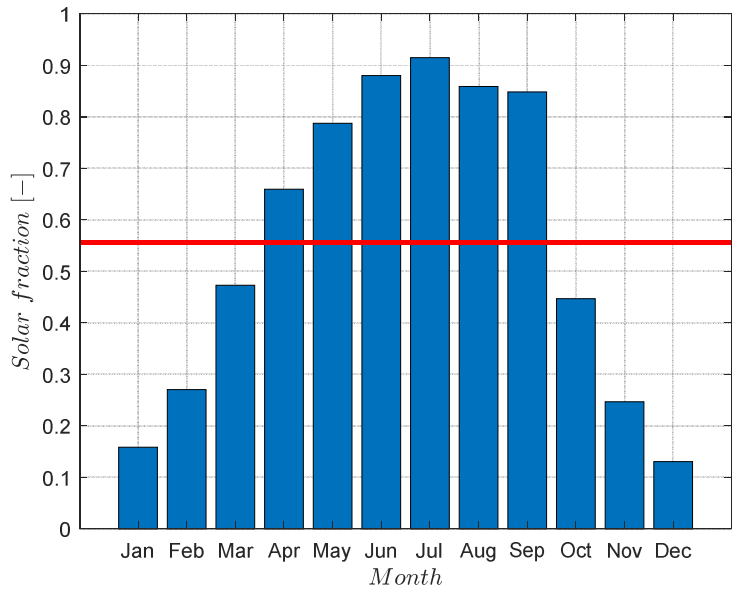

Figure 20 – Yearly solar coverage rate from model's simulation

The average solar coverage rate (red line) is equal to 56% and reaches a maximum value of about 90% in July, during which the collector is able to satisfy almost entirely the demand for DHW. The lowest value is instead recorded in the month of December, where the solar fraction does not exceed 15%. The values obtained can be considered consistent with similar systems adopted for the production of domestic hot water in locations with similar climate condition, where the solar fraction is between 40% and 60% (Mussard, 2017).

With the same monthly approach, the stored fraction f_{STORED} was evaluated. Figure 21 collects the trend of f_{STORED}.

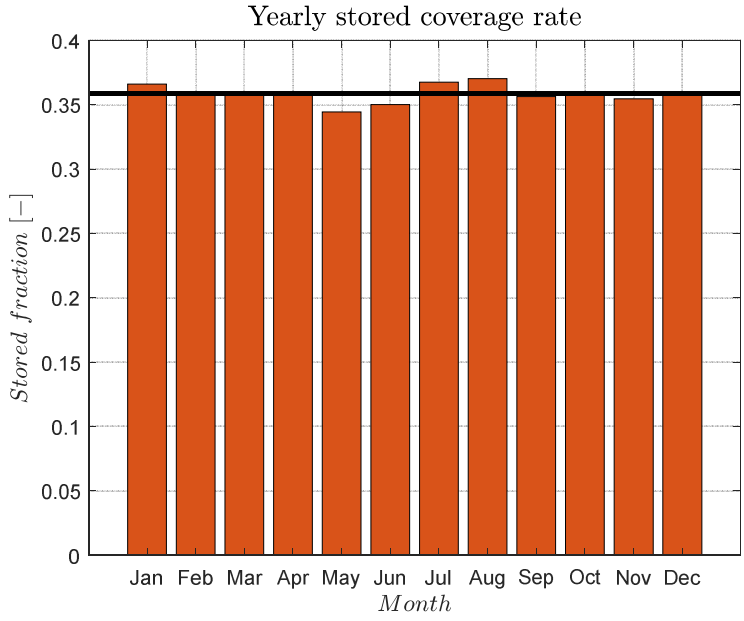

Figure 21 – Yearly stored coverage rate (stored fraction)

The fraction of energy accumulated during the year is rather constant, indicating that this value is not influenced by the outdoor weather condition. However, the average value, equal to 35.9% (black line), means that only one third of the solar radiation is effectively stored inside the prototype.

Focusing to the dynamic behaviour of the model, one day belonging to the summer season was taken into consideration. The model variable that has been analysed is the front plate cavity temperature (T_{pe}), that is the front plate of the PCM storage in direct contact with the domestic hot water exchange coil. The trend of this temperature is interesting since it is very variable when the water collection occurs.

Figure 22 represents the trend of the front cavity temperature (T_{pe}) during two typical days of the summer season (a) and winter season (b). Two DHW collection processes, set in the model between 6:00 and 8:00 and 18:00 and 20:00 are clearly visible in the graph, causing a lowering of the temperature of the front plate. The figure also shows the temperatures at the inlet (T_{in}) and at the outlet (T_{out}) of the DHW exchange coil are reported by the blue and red lines respectively. The water collection profile is described by the dotted black line and is equal to 0.5 l/min for both collection periods. In the figure it can also be noticed the areas where the PCM phase change occurs, at different temperatures depending on how the process takes place (solidification or fusion). The physical state of the PCM affects the heat exchange between the cavity and the water, undergoing a greater temperature drop when the material exchanges in the liquid phase. Finally, the external temperature (T_{ext}) was represented by the black dashed line.

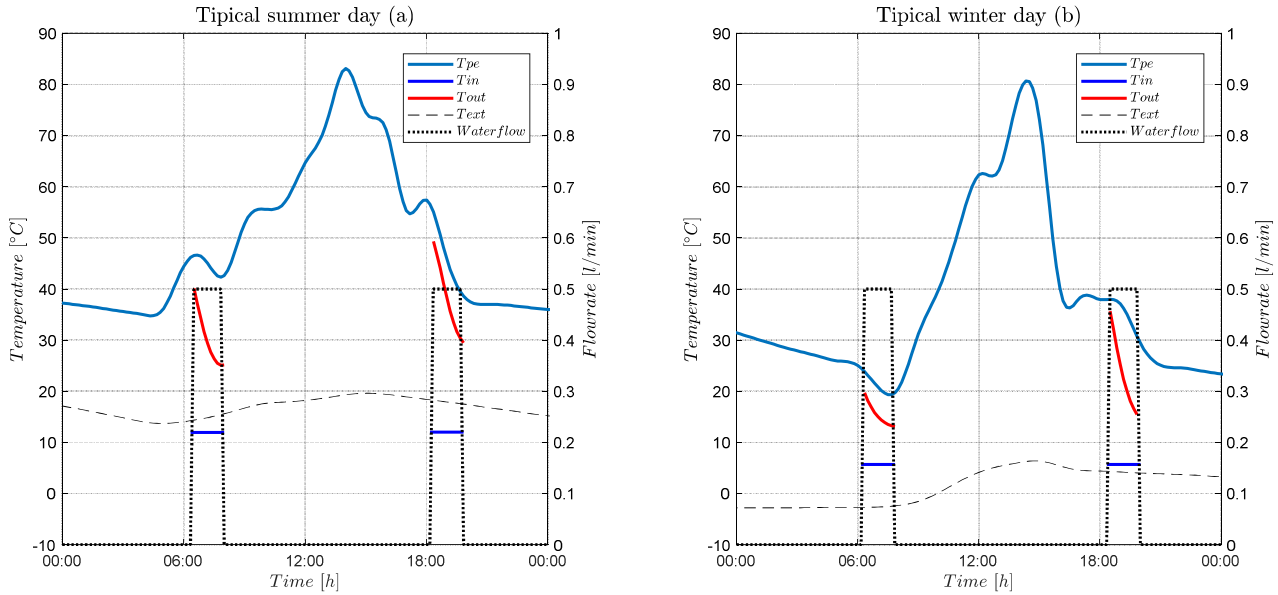

Figure 22 – Temperatures and waterflow trends on a typical summer (a) and winter (b) day extracted from the yearly model simulation

6. Conclusions

An innovative integrated collector storage (ICS) prototype for DHW production has been examined. The concept proposed is the first in the literature to integrate heat pipes with a PCM storage inside a fully insulated aluminium casing. This study made it possible to evaluate the global yearly performance of the prototype, identifying its main energy yields and productivity. A numerical model was developed in the EES environment and validated based on a previous experimental analysis. The prototype was modelled using an electrical analogy approach. A one-dimensional approach was used to model all the layers that make up the collector except the storage cavity containing the PCM, that was modelled with a two-dimensional mesh. Where there was a lack of data for modelling, specific hypotheses were put forward, based on the data collected during the previous experimental analysis. Particular attention was paid to the development of the model that describes the heat exchange established between PCM, cavity and DHW heat exchanger. A differential scanning calorimetry (DSC) analysis was performed to characterize PCM thermal behaviour. The model was then validated by means of the experimental data previously collected.

The yearly simulation results obtained show an average solar fraction of 56% and a productivity equal to 402.2 kWh/m^2, fully in line with commercial products. The dynamic behaviour of the prototype is also well predicted by the model, even though model response during a water collection has yet to be improved.

This study made it possible to test a non-commercial ICS prototype with remarkable innovative features. Compared to ICS systems already analysed in the literature, the behaviour of the prototype in harsh climates such as the one tested has been satisfactory and the thermal losses are not as negative as expected. The numerical simulations have clearly shown the effectiveness of the engineering choices adopted. The energy efficiency of the system is still slightly lower than that recorded in similar systems and the solar contribution is not yet exploited to its full potential, especially when the radiation involved is high. Nonetheless and overall, this new ICS compares favourably with conventional systems.

More research using different experimental scenarios might be needed to optimize the current model. Further studies can be developed to describe in more detail, especially at the numerical level, the phase transition of PCM. This is the aspect of modelling that requires greater attention because it represents the situation where numerical validation has room for improvement. Moreover, another aspect that could be relevant for future study concerns the simulation of the model in climates different from the one in which it was validated and experimentally tested here.

Overall, this study demonstrated the potential of the numerical model developed in the prediction of the physical behaviour of the case study. The adopted methodology made it also possible to confirm that analysed prototype of ICS is a potentially competitive collector with the state of the art.

Acknowledgements

This study has been supported and funded by the “Agence de l’Environnement et de la Maîtrise de l’Energie” (ADEME), under grant agreement N° 1205C0129. Partners: LOCIE, INSULA, SMCI, DATE

References

AL-Khaffajy, M., Mossad, R., 2013. Optimization of the heat exchanger in a flat plate indirect heating integrated collector storage solar water heating system. Renew. Energy 57, 413–421. https://doi.org/10.1016/j.renene.2012.11.033

Azzolin, M., Mariani, A., Moro, L., Tolotto, A., Toninelli, P., Del Col, D., 2018. Mathematical model of a thermosyphon integrated storage solar collector. Renew. Energy 128, 400–415. https://doi.org/10.1016/J.RENENE.2018.05.057

Bony, J., Citherlet, S., 2007. Numerical model and experimental validation of heat storage with phase change materials. Energy Build. 39, 1065–1072. https://doi.org/10.1016/j.enbuild.2006.10.017

Carmona, M., Palacio, M., 2019. Thermal modelling of a flat plate solar collector with latent heat storage validated with experimental data in outdoor conditions. Sol. Energy 177, 620–633. https://doi.org/10.1016/J.SOLENER.2018.11.056

Cruz, J.M.S., Hammond, G.P., Reis, A.J.P.S., 2002. Thermal performance of a trapezoidal-shaped solar collector/energy store. Appl. Energy 73, 195–212. https://doi.org/10.1016/S0306-2619(02)00061-2

D’Avignon, K., Kummert, M., 2016. Experimental assessment of a phase change material storage tank. Appl. Therm. Eng. 99, 880–891. https://doi.org/10.1016/j.applthermaleng.2016.01.083

Delcroix, B., Kummert, M., Daoud, A., 2015. Thermal behavior mapping of a phase change material between the heating and cooling enthalpy-temperature curves. Energy Procedia 78,

225–230. https://doi.org/10.1016/j.egypro.2015.11.612

Dharuman, C., Arakeri, J.H., Srinivasan, K., 2006. Performance evaluation of an integrated solar water heater as an option for building energy conservation. Energy Build. 38, 214–219. https://doi.org/10.1016/J.ENBUILD.2005.05.007

Dumas, J.P., Gibout, S., Cézac, P., Franquet, E., 2018. New theoretical determination of latent heats from DSC curves. Thermochim. Acta. https://doi.org/10.1016/J.TCA.2018.10.011

Ecevit, A., Al-Shariah, A.M., Apaydin, E.D., 1989. Triangular built-in-storage solar water heater. Sol. Energy 42, 253–265. https://doi.org/10.1016/0038-092X(89)90016-9

Esen, M., Esen, H., 2005. Experimental investigation of a two-phase closed thermosyphon solar water heater. Sol. Energy 79, 459–468. https://doi.org/10.1016/j.solener.2005.01.001

European Union, 2018. Directive (EU) 2018/ of the European Parliament and of the Council of 30 May 2018 amending Directive 2010/31/EU on the energy performance of buildings and Directive 2012/27/EU on energy efficiency. Off. J. Eur. Union 2018, 75–91.

Fraisse, G., Pailha, M., 2016. Etude numérique et expérimentale d'un nouveau concept de capteur solaire thermique auto-stockeur à changement de phase, in: Journées Nationales Sur l'Energie Solaire.

Garg, H.P., 1975. Year round performance studies on a built-in storage type solar water heater at Jodhpur, India. Sol. Energy 17, 167–172. https://doi.org/10.1016/0038-092X(75)90055-9

Ge, T.S., Wang, R.Z., Xu, Z.Y., Pan, Q.W., Du, S., Chen, X.M., Ma, T., Wu, X.N., Sun, X.L., Chen, J.F., 2017. Solar heating and cooling: Present and future development. Renew. Energy 126, 1126–1140. https://doi.org/10.1016/j.renene.2017.06.081

Haillot, D., Goetz, V., Py, X., Benabdelkarim, M., 2011. High performance storage composite for the enhancement of solar domestic hot water systems. Part 1: Storage material investigation. Sol. Energy 85, 1021–1027. https://doi.org/10.1016/j.solener.2011.02.016

Haillot, D., Nepveu, F., Goetz, V., Py, X., Benabdelkarim, M., 2012. High performance storage composite for the enhancement of solar domestic hot water systems. Part 2: Numerical system analysis. Sol. Energy 86, 64–77. https://doi.org/10.1016/j.solener.2011.09.006

Helal, O., Chaouachi, B., Gabsi, S., 2011. Design and thermal performance of an ICS solar water heater based on three parabolic sections. Sol. Energy 85, 2421–2432. https://doi.org/10.1016/J.SOLENER.2011.06.021

IEA, 2018a. Global Energy & CO 2 Status Report.

IEA, 2018b. Annex 31 - Energy Storage with Energy Efficient Buildings and Districts: Optimization and Automation.

Kaushik, S.C., Kumar, R., Garg, H.P., Prakash, J., 1994. Transient analysis of a triangular built-in-storage solar water heater under winter conditions. Heat Recover. Syst. CHP 14, 337–341. https://doi.org/10.1016/0890-4332(94)90037-X

Khan, M.Z., 2016. Analysis and Modelling of Single Slope Solar Still at Different Water Depth. J. Energy Technol. Policy 6, 1–4.

Kumar, N., Chavda, T., Mistry, H.N., 2010. A truncated pyramid non-tracking type multipurpose domestic solar cooker/hot water system. Appl. Energy 87, 471–477. https://doi.org/10.1016/J.APENERGY.2009.06.031

Kumar, R., Rosen, M.A., 2010. Thermal performance of integrated collector storage solar water heater with corrugated absorber surface. Appl. Therm. Eng. 30, 1764–1768. https://doi.org/10.1016/j.applthermaleng.2010.04.007

Kuznik, F., Virgone, J., Roux, J.J., 2008. Energetic efficiency of room wall containing PCM

wallboard: A full-scale experimental investigation. Energy Build. 40, 148–156. https://doi.org/10.1016/j.enbuild.2007.01.022

Ministère de l'Egalité des Territoires et du Logement, 2013. Réglementation thermique 2012, version modifiée avril 2013. J. Off. la République française 12.

Mussard, M., 2017. Solar energy under cold climatic conditions: A review. Renew. Sustain. Energy Rev. 74, 733–745. https://doi.org/10.1016/J.RSER.2017.03.009

Nemec, P., Caja, A., Malcho, M., 2011. Thermal Performance Measurement of Heat Pipe. Glob. J. Technol. Optim. 2, 104–110.

REN21, 2018. Renewables 2018: Global Status Report.

REN21, 2014. Renewable 2014: Global Status Report.

Robinson, B.S., Chmielewski, N.E., Knox-Kelecy, A., Brehob, E.G., Sharp, M.K., 2013. Heating season performance of a full-scale heat pipe assisted solar wall. Sol. Energy 87, 76–83. https://doi.org/10.1016/j.solener.2012.10.008

Robinson, B.S., Sharp, M.K., 2015. Reducing unwanted thermal gains during the cooling season for a solar heat pipe system. Sol. Energy 115, 16–32. https://doi.org/10.1016/j.solener.2015.02.011

Serale, G., Fabrizio, E., Perino, M., 2015. Design of a low-temperature solar heating system based on a slurry Phase Change Material (PCS). Energy Build. 106, 44–58. https://doi.org/10.1016/j.enbuild.2015.06.063

Singh, R., Lazarus, I.J., Souliotis, M., 2016. Recent developments in integrated collector storage (ICS) solar water heaters: A review. Renew. Sustain. Energy Rev. 54, 270–298. https://doi.org/10.1016/j.rser.2015.10.006

Smyth, M., Eames, P.C., Norton, B., 2006. Integrated collector storage solar water heaters. Renew. Sustain. Energy Rev. 10, 503–538. https://doi.org/10.1016/j.rser.2004.11.001

Souliotis, M., Tripanagnostopoulos, Y., 2004. Experimental study of CPC type ICS solar systems. Sol. Energy 76, 389–408. https://doi.org/10.1016/j.solener.2003.10.003

Tripanagnostopoulos, Y., Souliotis, M., 2004. ICS solar systems with horizontal (E-W) and vertical (N-S) cylindrical water storage tank. Renew. Energy 29, 73–96. https://doi.org/10.1016/S0960-1481(03)00144-7

Appendix A. Cavity electrical analogy scheme

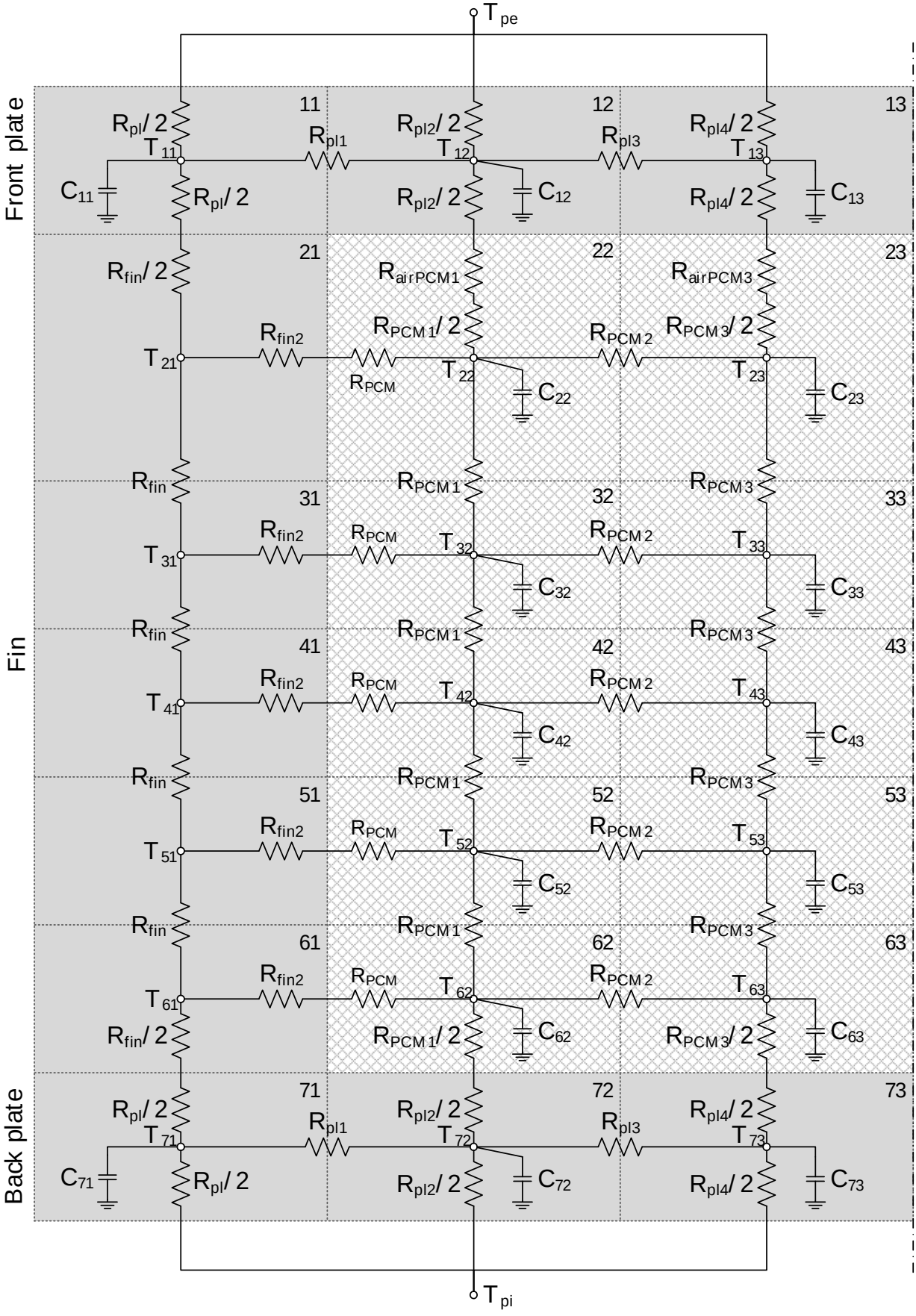

Figure A-1 - Cavity: electrical analogy model